Icarus 211 (2011) 722–731

Contents lists available at ScienceDirect

Icarus

journal homepage: www.elsevier.com/locate/icarus

Wave constraints for Titan's Jingpo Lacus and Kraken Mare from VIMS specular reflection lightcurves

Jason W. Barnes [a,*], Jason M. Soderblom [b], Robert H. Brown [b], Laurence A. Soderblom [c], Katrin Stephan [d], Ralf Jaumann [d], Stéphane Le Mouélic [e], Sebastien Rodriguez [f], Christophe Sotin [g], Bonnie J. Buratti [g], Kevin H. Baines [g], Roger N. Clark [h], Philip D. Nicholson [i]

[a] Department of Physics, University of Idaho, Moscow, ID 83844-0903, United States
[b] Department of Planetary Sciences, University of Arizona, Tucson, AZ 85721, United States
[c] United States Geological Survey, Flagstaff, AZ 86001, United States
[d] DLR, Institute of Planetary Research, Rutherfordstrasse 2, D-12489 Berlin, Germany
[e] Laboratoire de Planétologie et Géodynamique, CNRS UMR6112, Université de Nantes, France
[f] Laboratoire AIM, Centre d'étude de Saclay, DAPNIA/Sap, Centre de l'Orme des M erisiers, bât. 709, 91191 Gif/Yvette Cedex, France
[g] Jet Propulsion Laboratory, California Institute of Technology, 4800 Oak Grove Drive, Pasadena, CA 91109, United States
[h] United States Geological Survey, Denver, CO 80225, United States
[i] Department of Astronomy, Cornell University, Ithaca, NY 14853, United States

ARTICLE INFO

Article history:
Received 15 April 2010
Revised 18 September 2010
Accepted 28 September 2010
Available online 7 October 2010

Keywords:
Titan
Photometry
Satellites, surfaces

ABSTRACT

Stephan et al. (Stephan, K. et al. [2010]. Geophys. Res. Lett. 37, 7104–+.) first saw the glint of sunlight specularly reflected off of Titan's lakes. We develop a quantitative model for analyzing the photometric lightcurve generated during a flyby in which the specularly reflected light flux depends on the fraction of the solar specular footprint that is covered by liquid. We allow for surface waves that spread out the geographic specular intensity distribution. Applying the model to the VIMS T58 observations shows that the waves on Jingpo Lacus must have slopes of no greater than 0.15°, two orders of magnitude flatter than waves on Earth's oceans. Combining the model with theoretical estimates of the intensity of the specular reflection allows a tighter constraint on the waves: $\leqslant$0.05°. Residual specular signal while the specular point lies on land implies that either the land is wetted, the wave slope distribution is non-Gaussian, or that 5% of the land off the southwest edge of Jingpo Lacus is covered in puddles. Another specular sequence off of Kraken Mare acquired during *Cassini*'s T59 flyby shows rapid flux changes that the static model cannot reproduce. Points just 1 min apart vary in flux by more than a factor of two. The present dataset does not uniquely determine the mechanism causing these rapid changes. We suggest that changing wind conditions, kilometer-wavelength waves, or moving clouds could account for the variability. Future specular observations should be designed with a fast cadence, at least 6 points per minute, in order to differentiate between these hypotheses. Such new data will further constrain the nature of Titan's lakes and their interactions with Titan's atmosphere.

1. Introduction

Specular reflections have long been considered to be a mechanism by which to identify liquid surfaces on Saturn's moon Titan. Earth-based radar observations by Campbell et al. (2003) detected specular returns from the equatorial regions prior to Cassini's arrival. The geographic location of those returns, within Titan's tropics, however, have been subsequently revealed to be desert. We still do not understand the mechanism that generates these equatorial specular radar signals. They may result from surfaces that are very flat at radar wavelengths, such as dry lakebeds (playas), or from reflections of a flat subsurface methane aquifer.

Stofan et al. (2007) first found evidence for surface liquids from Cassini. In a way, these observations relied on a specular reflection. Unlike the Earth-based observations, which showed a positive indication of a specular signal, the Cassini RADAR lake detection is based on NOT detecting any reflected signal at all, specular or diffuse. The synthetic aperture radar cross-section over the northern lakes is so low that Stofan et al. (2007) inferred that the off-nadir RADAR pulse was being specularly reflected away from the spacecraft, leaving no diffusely scattered RADAR return signal from the surface. Recently Wye et al. (2009) confirmed a specular RADAR reflection from Ontario Lacus in the Cassini RADAR's nadir-looking altimetry mode.

Surface liquids also produce specular reflections in optical and near-infrared wavelengths. Without active illumination, observing such reflections requires sunlight, and thus particular observing

* Corresponding author. ResearcherID number: B-1284-2009.
E-mail address: jwbarnes@uidaho.edu (J.W. Barnes).

0019-1035/$ - see front matter © 2010 Elsevier Inc. All rights reserved.
doi:10.1016/j.icarus.2010.09.022

geometries. Observations at these shorter wavelengths should be less susceptible to false positives caused by smooth solid surfaces. West et al. (2005) found no specular signal when observing Titan from Earth in the 2-μm atmospheric window. But the limited Earth–Titan–Sun geometry necessarily limits telescopic specular observations to Titan's tropics.

Fussner (2006) in an unpublished masters thesis used *Cassini* Imaging Science Subsystem (ISS) images to search for specular reflections on Titan's surface at 0.938 μm. She did not find any. Once again, however, the geometries available for that study sampled mostly equatorial latitudes due to Cassini's mission-designed trajectory for the early Titan flybys. Furthermore, the Sun was below the horizon in the northern lake district (e.g. Barnes et al., 2009), so detection of a specular reflection was, in retrospect, not possible.

Recently, Stephan et al. (2010) discovered a dramatic specular reflection from a north-polar Mare using *Cassini* Visual and Infrared Mapping Spectrometer (VIMS) at 5 μm seen during the high-phase sequence obtained on Cassini's T58 ingress. The observations comprise four VIMS cubes acquired over the course of 2 h. The cubes show the specular reflection in adjacent bright pixels with I/F of nearly 3 at their maximum (I/F is defined as the measured flux from a surface divided by the theoretical flux from a Lambertian reflector with an albedo of 1.0 at the same distance from the Sun). Despite VIMS' continuous wavelength coverage between 0.3 μm and 5.2 μm, the specular reflection is not visible within any of the shorter wavelength atmospheric windows. Stephan et al. (2010) used radiative transfer models to establish that few enough photons remain unscattered in the shorter windows that, for the extant viewing geometry, specular reflections should only have been visible from space at longer wavelengths near the 5 μm window. Soderblom et al. (2010) derive the analytical characteristics and behavior of the solar specular reflection's geometry and intensity.

Macroscopic sea surface roughness – in the form of ripples and waves – affects an observed specular geographic footprint's intensity distribution. The seminal work on the topic based on observations of Earth's oceans from an airplane was done by Cox and Munk (1954). The roughness can be considered as a multitude of individual tilted surface facets. Each facet has a different specular geometry, leading to a specular reflection in different geographic locations based on the facet's orientation. As a result rough seas have wider, lower-intensity specular footprints than calmer seas. A perfectly smooth, glass-like, sea surface would produce a perfect image of the Sun in reflection (for an uncurved surface).

The topic of specular reflections off of roughened liquids has recently become of interest with the discovery of extraterrestrial seas, both in the context of Titan and that of oceans on hypothetical extrasolar planets (Williams and Gaidos, 2008; Cowan et al., 2009; Oakley and Cash, 2009). In this paper we further analyze the four-point photometric lightcurve from the VIMS T58 specular observation described by Stephan et al. (2010) to quantitatively constrain the surface properties of Jingpo Lacus and its environs. In Section 2 we describe the model that we have developed to generate theoretical specular lightcurves based on Synthetic Aperture RADAR (SAR) imaging and observation geometry. Next we fit the VIMS T58 data with a least-squares minimization technique in Section 3 to measure critical parameters, including the distribution of surface normals (roughness). In Section 4 we extend our investigation to a separate VIMS specular sequence acquired on the T59 flyby before concluding.

2. Model

The Cox and Munk (1954) airborne results describe spatially resolved solar specular reflections off of Earth's oceans. They inferred sea-surface topography characteristics from the brightness distribution of the specular footprint. Because the VIMS T58 specular observations are not spatially resolved, the precise Cox and Munk (1954) approach will not work to analyze the Titan data.

The T58 observations are, however, *temporally* resolved. As the specular footprint moves across Titan's geography, it samples surfaces with different specular properties. Given some information regarding the spatial distribution of units with distinct specular reflective properties, it is possible to then infer the spatial properties of the specular reflection from the lightcurve. The process is similar to that used in the extrasolar planet community to characterize transiting planets from a photometric lightcurve, despite the planet and star themselves being spatially unresolved (e.g. Barnes and Fortney, 2004).

To quantitatively analyze the VIMS T58 observations (Fig. 1), we develop a model that can generate a theoretical lightcurve for a sequence of time given the *Cassini*–Titan–Sun geometry and a set of characteristic parameters. We obtain geometric information from the set of reconstructed *Cassini* SPICE (Acton, 1999) kernels for the time in question. The specular footprint depends only on the spacecraft's position relative to Titan and the Sun. It does not depend on the spacecraft's orientation or instrument pointing.

We first calculate the geographic location of the specular point. At the specular point, and only at the specular point, the local surface normal is parallel to the mean of the incidence and emission unit vectors (see Fig. 2). We determine the specular point iteratively, calculating the surface normal and mean of the incidence and emission vectors separately for an initial latitude and longitude. We then use the Press et al. (2007) two-dimensional `amoeba` algorithm to minimize the angle between the two vectors.

To start, we use the Spacecraft Planet Instrument Pointing Events (SPICE) kernels to calculate the vector to the Sun, $\vec{S}$, and to *Cassini*, $\vec{C}$, in a Titan-centric coordinate system. For each iteration, we use the test point latitude and longitude to determine the vector to the candidate surface point, $\vec{P}$. The algorithm assumes Titan to be a triaxial ellipsoid with axes a, b, and c for the sub-Saturn, leading–trailing, and polar radii, respectively.

For the Jingpo Lacus observation we assume that $a = b = c = 2574.0$ based on the SARtopo estimate of the absolute lake elevation (Randolph Kirk, personal communication). This

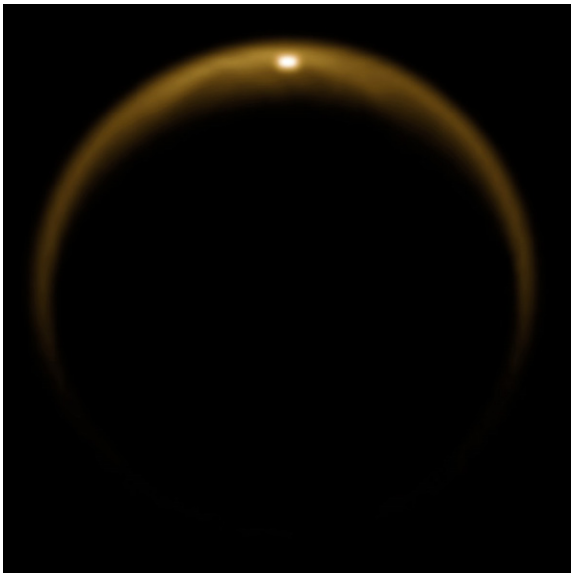

Fig. 1. VIMS view of the specular glint off of Jingpo Lacus on the T58 flyby (Stephan et al., 2010). This is a monochromatic 5-μm image, colorized for dramatic effect. This particular cube is referred to as point #3 in the text. This image has been Lanczos interpolated from its original 64 × 64 pixel format.

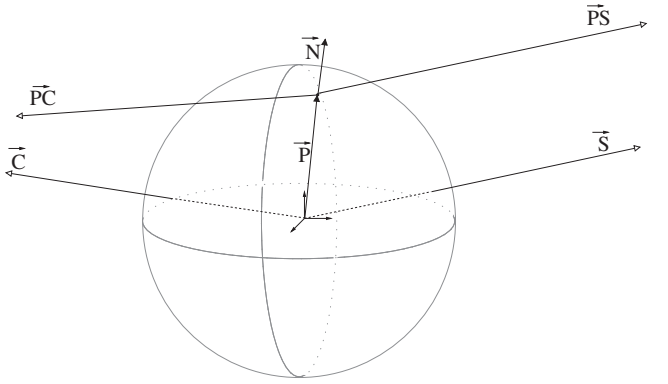

Fig. 2. Diagram showing the geometry of the specular reflection problem as discussed in Section 2.

elevation is below that of the moon's triaxial figure as determined by Zebker et al. (2009); the difference arises from Jingpo's location at a local minimum below the surrounding topography. At any rate, the specular location shift caused by changing the local radius by less than a kilometer is negligible.

Given the distances involved, our calculated specular position would be incorrect if we were to use the vectors S and C as calculated from Titan's center (though using $\vec{S}$ from Titan's center would be a quite good approximation). We therefore use the vector from the surface point to the Sun, $\vec{PS} \equiv \vec{S} - \vec{P}$, and the vector from the surface point to *Cassini*, $\vec{PC} \equiv \vec{C} - \vec{P}$, instead. The surface point is specular if the sum of the unit vectors $\widehat{PS}$ and $\widehat{PC}$ points in the direction of the surface normal, $\widehat{N}$. The algorithm assesses the specular point to be the one where the angle between $\widehat{N}$ and $\widehat{PS} + \widehat{PC}$ is zero. Refraction by Titan's atmosphere can be ignored if Titan's atmosphere is assumed to be locally invariant with latitude and longitude (Soderblom et al., 2010).

To calculate the specular footprint of the solar disk, we find the Sun's edge by rotating $\vec{S}$ vector by the Sun's angular radius (0.05°). Then we rotate the edge vector around $\vec{S}$ to define a set of edge points (usually 30). We calculate the specular point on the surface for each of those edge points separately, and assign the solar disk footprint as a filled polygon defined by the set of these specular points. For a perfectly smooth sea, the solar footprint defines the distribution of specular reflection. We assume no solar limb-darkening, which is a very good (Seager and Mallén-Ornelas, 2003) but not perfect (e.g., Knutson et al., 2007; Agol et al., 2010) assumption at 5 μm.

For a roughened sea surface, the distribution of specular reflection is spread out by an amount that depends on the two-dimensional distribution of surface facets. Cox and Munk (1954) found that the surface facets on Earth's oceans fit a symmetric Gaussian distribution reasonably well. Therefore we assume a two-dimensional Gaussian distribution of surface facets with a tunable characteristic width σ in radians which corresponds to the average slope on the sea surface. To simulate the geographic flux distribution for the specular reflection of a point-source Sun, we assemble a series of uniform "tuna-can" distributions with progressively larger angular width (Fig. 6, assigning the intensity of each new annulus the Gaussian intensity for that corresponding angle relative to σ (see Fig. 3, top). We determine the geographic boundaries of each tuna-can with a method similar to that for finding the Sun's footprint. We assemble a 30-point polygon of angular deviations from the local surface normal that are equal in magnitude but have directions that vary in a circle. Then we find the specular points for each of those polygon vertices by incorporating that deviation from the local surface normal in the iterative specular algorithm described above.

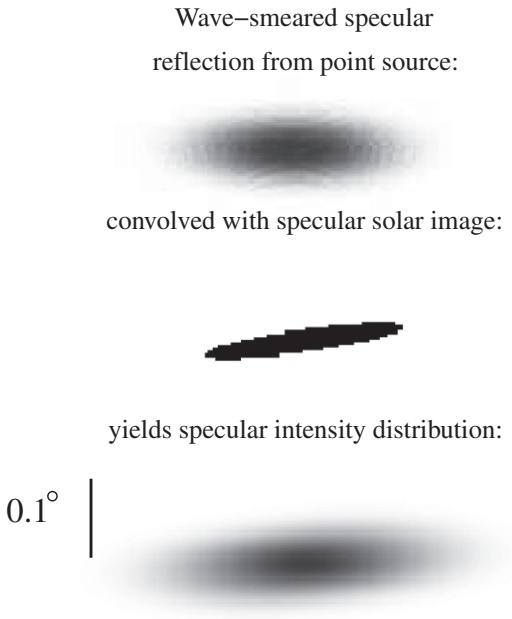

Fig. 3. This diagram shows a visual representation of the wave convolution process for an assumed Gaussian wave distribution with $\sigma = 0.05°$ on T58. Each of the images appears as in a cylindrical map centered on southwestern Jingpo Lacus. The Sun is to the south-southeast in this image, and the spacecraft direction is toward the north-northwest, causing the tilted image. The image is squeezed along the specular reflection direction because wave tilt in the direction of the reflection are amplified by a factor of two because in increases both the angle of incidence and the angle of reflection by the same amount.

In the extended-source case with facet distributions with σ similar to the angular diameter of the Sun, the surface distribution is more difficult to calculate. The geographic specular flux distribution could then be calculated by determining the fraction of facets in each pixel whose geometry is specular. Explicitly calculating the fraction of each pixel that is specular with respect to an extended-source Sun separately, however, becomes computationally prohibitive.

Instead, we approximate the distribution as a convolution of the solar footprint and the facet distribution footprint for a point source (Fig. 3). This approximation breaks down only when the geometry changes significantly over the relevant Titan surface positions. Given the small angles and differences in latitude and longitude involved with the T58 observation, the errors introduced by the approximation are well less than the errors that result from having quantized pixels in the calculation instead of a continuum. For facet distributions whose deviation from the local surface normal is much greater than the apparent angular size of the Sun, the resulting surface specular intensity distribution becomes indistinguishable from that of the facet distribution itself.

The Sun as viewed from Titan is ~0.05° (1 milliradian) across. Hence for wave facet distributions with width of order ~0.05° we convolve the facet distribution footprint with the solar footprint to arrive at a suitable representation of the true specular intensity distribution.

To further speed the forward calculation, we also assume that the geographic distribution of the net specular reflection does not change relative to the spectral point of the center of the Sun over the course of the observation (i.e., that the shape of the spot does not change). The speedup is not necessary when calculating an individual lightcurve, but it improves the computation time for the least-squared fits by a hundredfold.

3. Jingpo Lacus

3.1. Model fits

Four separate cubes comprise the VIMS T58 specular observations (Stephan et al., 2010). The specular reflection is visible only within the 5-μm atmospheric window; hence we use data from this window exclusively in our analysis. The total elapsed time from the first to the last cube is 2.25 h. Points 1 and 2 are ~20 min apart, followed by a long gap of ~2 h, and then points 3 and 4 are another ~20 min apart. For details about each T58 observation see Stephan et al. (2010) and Table 1.

For each cube the specular reflection is spread over 2 adjacent pixels by the instrumental point spread function. The specular intensity distribution is not spatially resolved. In order to separate the specular contribution within the two specular pixels, we sum the two specular pixels and then subtract off the values of the two neighboring pixels with similar phase angle as a proxy for the background (see Fig. 4). The other surrounding pixels have significantly different geometry with VIMS' large pixels in this crescent view, and are not good representations of the non-specular background (see Fig. 5). The resulting lightcurve can be seen as the data points marked with a '*' in Figs. 7 and 8. Because we assume that the background pixels are free of specular reflection and that no other pixels contain any specular flux, our measured values may not represent the entirety of the specular signal.

We think that the dominant noise source for each photometric data point is likely this background subtraction step. Therefore we assign error bars to each measurement based on the difference between the two pixels from which we derive the background. The time assigned to each observation corresponds to the time at which the brightest of the two specular pixels was acquired by the instrument (the total time difference between the two is equal to the image's X dimension plus 1 times the integration time – i.e. from 1.5 up to 42 s depending on the cube).

The specular point on Titan lies, at those times, in the southwestern end of a lake that the IAU has named Jingpo Lacus. It is named after Jingpo lake in China, whose name means "Mirror", in reference to this observation. This lake is ~200 km in length from north to south, and perhaps ~70 km wide (Fig. 9). RADAR has shown almost all of the shoreline, but the eastern margin has not yet been mapped. The lake's center is 73N 24E. It lies to the west of Kraken Mare.

Fig. 10 shows the location and shape of the specular solar images for each of the points. Each of points 1–3 lies near an apparent shoreline in the RADAR view. Hence with wave smearing, different amounts of the specular intensity pattern will fall on land relative to that on liquid. We assume that RADAR pixels with reflectivity $\leqslant 0.05$ correspond to liquid surfaces, and the rest to solid surfaces that produce no specular reflection. While changes in the location of the Jingpo Lacus shoreline between T19 and T58 are possible given evidence for lake-level changes in Ontario Lacus (Barnes et al., 2009), the steeper slopes of Jingpo's jagged shoreline imply that lake-level changes of similar magnitude would affect this lake less than shallow Ontario. We median-filtered the T19 SAR image with a radius of 0.02° in order to smooth out RADAR's inherent speckle noise.

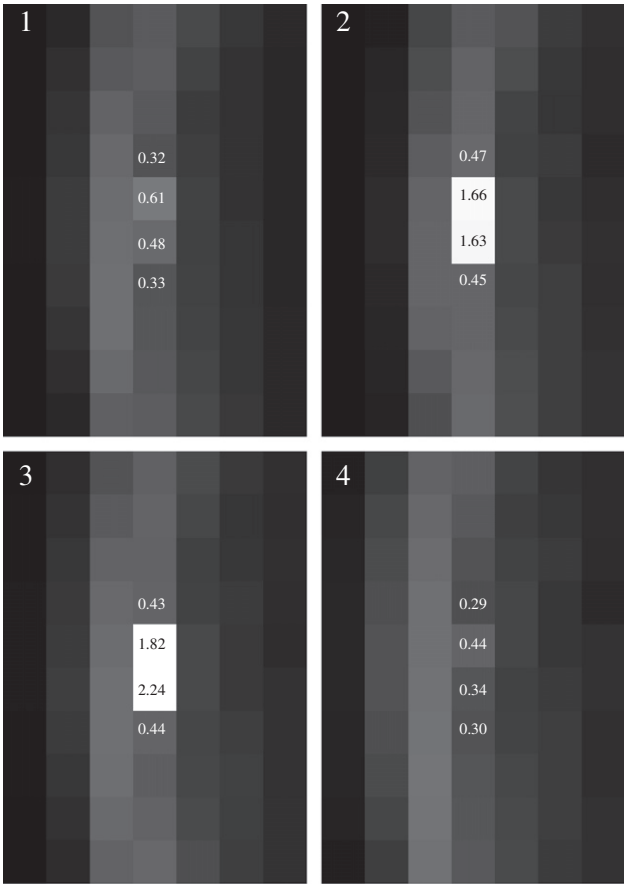

Fig. 4. Here we show the raw I/F values, coadded across the 16 VIMS channels in the 5-μm window, for VIMS cubes 1–4 from T58.

We then fit the four different photometric points as a timeseries in order to constrain wave activity. We leave the total maximum intensity of a pure liquid specular reflection as a free parameter in the fit. Although the RADAR maps use the updated position of Titan's rotational pole, the small residual shifts (of order a few RADAR pixels, or up to a kilometer) in our knowledge of the absolute location of the RADAR observations (Stiles et al., 2008) becomes significant when compared to the size of the specular footprint (also of order 1 km). We therefore also fit for the relative offset in latitude and longitude of the T19 RADAR strip.

We fix the wave facet distribution to be a Gaussian with a particular width σ each time that we fit the lightcurve. With just four data points, the reduced χ^2 would be meaningless if we were to fit for more than three parameters simultaneously. We use a Leavenberg–Marquardt χ^2 minimization algorithm from Press et al. (2007) to fit the data.

Figs. 7 and 8 show the best-fit lightcurves as a function of the characteristic wave angle σ, and the best-fit parameters are shown in Table 2. For $\sigma \leqslant 0.15°$ we find good fits to the data (Fig. 7). With waves having $\sigma \geqslant 0.20°$, the model cannot adequately reproduce the data, with fits using greater wave angles showing progressively worse fits (Fig. 8).

Table 1
VIMS specular observations.

Flyby	Date	Range (km)	$i = e$ (°)	Integration time (ms)	Geometry (pixels)	Cubes
T58	2009 July 8	233,500–194,300	73	160	52 × 52	2
				640	64 × 64	2
T59	2009 July 24	334,721–223,512	76–82	640	64 × 64	2
				640	48 × 48	3
				220	6 × 38	2
				220	6 × 42	4
				160	48 × 48	3
				80	64 × 64	1

Note: Since we are in the specular regime, the incidence angle (i) is equal to the emission angle (e), and the total phase angle $\varphi = i + e$.

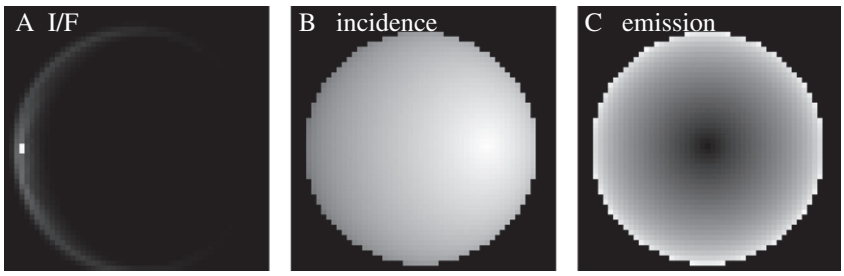

Fig. 5. Here we show (A) the raw I/F of 64 × 64 VIMS cube 2 from T58 in non-interpolated pixels; (B) the incidence angle for VIMS cube 2 from T58, stretched from 0° to 180°; and (C) the emission angle for VIMS cube 2 from T58, stretched from 0° to 90°. The gradient for both the incidence and emission angles is greatest from left-to-right across the image, so we use only the pixels to the top and bottom of the specular pixels to subtract off as background (see Fig. 4).

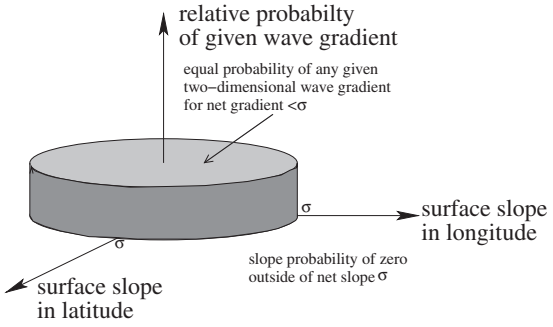

Fig. 6. Illustration of a "tuna-can" wave gradient probability distribution function.

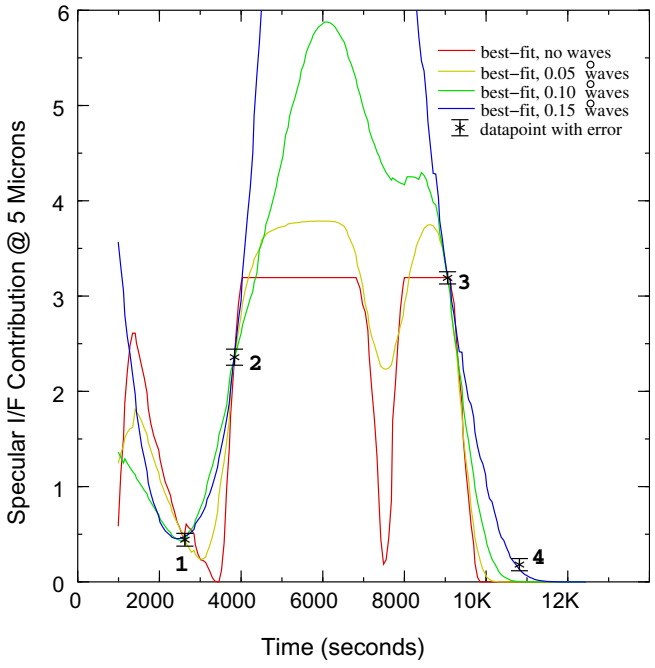

Fig. 7. The VIMS T58 specular lightcurve, along with best-fit curves for 2D Gaussian wave distributions as described in the text. This figure shows those wave distributions that for which the model can reproduce the observed data; those wave distribution that we can rule out are shown in Fig. 8. The 0.15° fit is cut-off at the top, but would extend up to an I/F of 18.

Fig. 11 depicts the location of the specular footprints and their intensity distributions for selected best-fit solutions. In the no-waves case, footprint 1 lies mostly on a peninsula of land, with just the northeastern corner on liquid in order to reproduce the relatively small specular flux from that point. Point 2 lies just to the

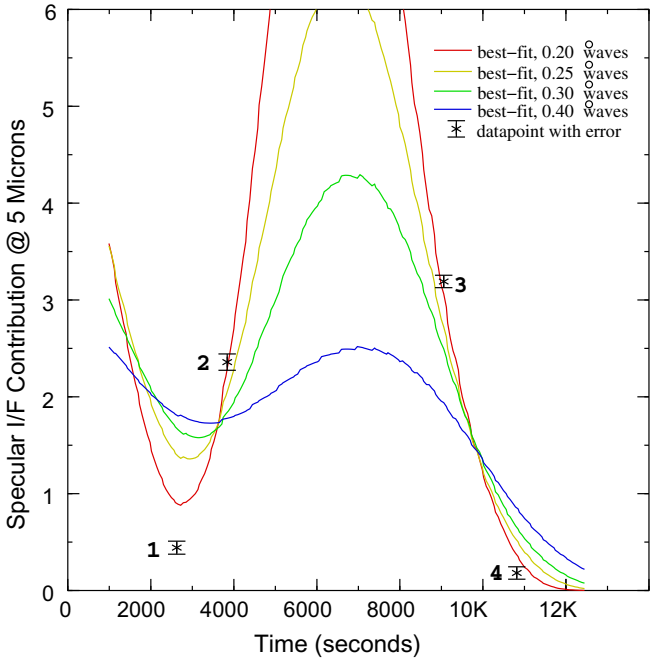

Fig. 8. The VIMS T58 specular lightcurve, along with best-fit curves for 2D Gaussian wave distributions as described in the text. This figure shows those wave distributions that for which the model is unable to adequately reproduce the observed data; we rule out waves of this size. Allowed wave fits are shown in Fig. 7. The jaggedness of the curves comes about due to granulation in the RADAR basemap used to determine whether each geographic location is liquid.

west of a shoreline with its easternmost portion falling on land. Point 3's slightly higher flux compared to point 2 gets reproduced with the footprint falling entirely on liquid surface. The best-fit curve goes through points 1–3, but misses point 4 because point 4 lies entirely on land.

For small waves with $0° < \sigma < 0.15°$ the specular intensity distribution on the surface becomes too large to be entirely on liquid. The fitting algorithm reproduces the lightcurve with these wave distributions by increasing the maximum intensity to compensate for the fractional loss of reflection on land. These fits are statistically indistinguishable in quality from the no-waves case (Fig. 12).

In the larger wave case, $\sigma > 0.15°$ (Fig. 8), the surface intensity distribution grows so wide that only a fraction of the specular footprint occurs over liquid at any given time. Because of this, the lightcurve model fit cannot change aggressively enough to simultaneously go through points 1 and 2 and points 3 and 4. Each of these points differ significantly from each other in specular flux, but their footprint centers lie only a few kilometers apart on the surface. The fits grow progressively worse with increasing σ (Fig. 12).

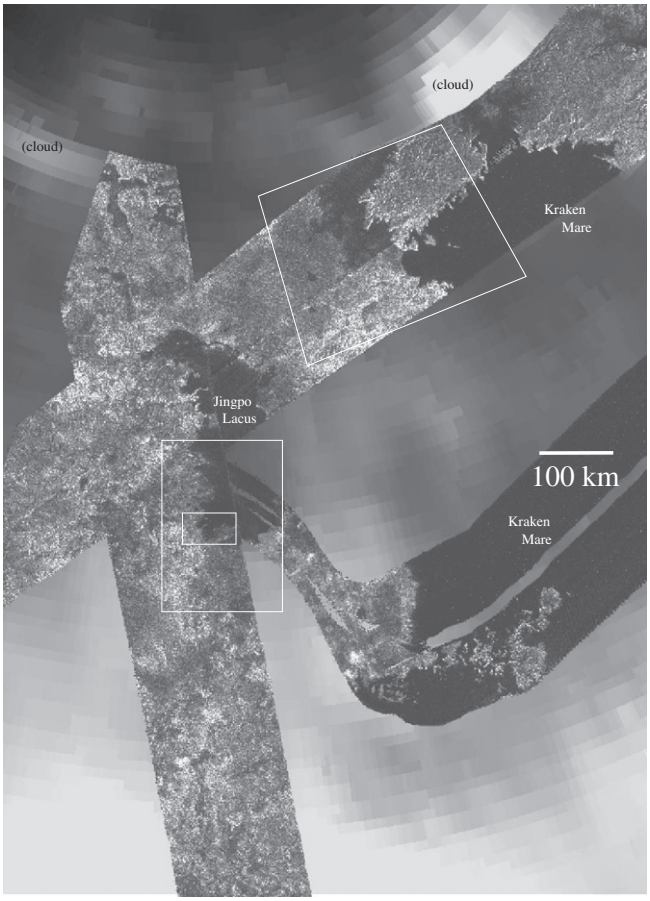

Fig. 9. Overview map of the Jingpo Lacus/Kraken Mare region near Titan's north pole. RADAR T19 (left), T28 (top), and T30 (bottom-right) are superposed on a VIMS 5-μm basemap from T54. The area is shown in orthographic projection from above Jingpo Lacus (73N 24E), with north directly to the top of Jingpo Lacus. The larger box at bottom left delineates the portion of southwestern Jingpo Lacus shown in Fig. 10; the smaller, inset bottom-left box delineates the T58 specular area of southwestern Jingpo Lacus shown in detail in Fig. 11; the top-right box delineates the T59 specular area of Kraken Mare shown in Fig. 14.

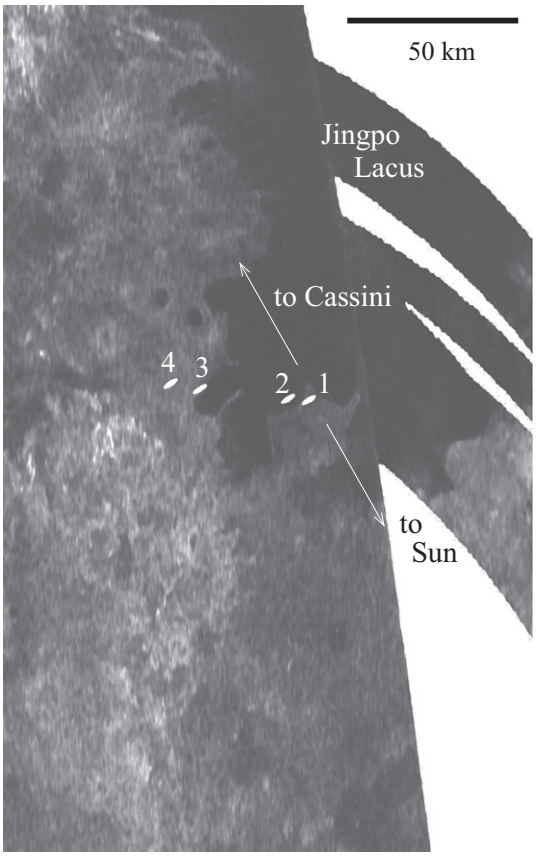

Fig. 10. This map shows southwestern Jingpo Lacus, giving a detailed look at the location of the solar specular footprints from T58 in context with a RADAR T19 SAR image. Points 1–3 are all in close proximity to shorelines. This is a cylindrical map that has been squeezed by a factor of 4 in longitude in order to more accurately represent shapes and areas at this northerly latitude (~71°N). The solar images are compressed in the down-Sun direction; see Soderblom et al. (2010) for the theory of specular images on planetary surfaces.

The χ^2 for the $\sigma = 0.15°$ case reaches a minimum. For this wave angle the algorithm can still fit points 1–3, barely, but now the surface distribution is wide enough to have a corner on liquid for point 4 as well. Hence this is the only Gaussian wave distribution that can simultaneously fit all four points. As discussed in the next section, however, this particular fit is suspect.

3.2. Implications

The bad fits for Gaussian wave distributions with $\sigma > 0.15°$ lead us to place an upper limit on the waves at southwestern Jingpo Lacus on T58 of $\sigma \leqslant 0.15°$. Based on our assumptions, the constraint applies only to waves with wavelength much smaller than the size of the solar specular image – a few km across. There are no other empirical constraints on the potential wavelength of the waves that VIMS would measure. Without knowledge of the wavelength, we cannot make a direct comparison between the VIMS gradient constraint and the Wye et al. (2009) measurement at Ontario Lacus in RADAR height constraint. They are both, however, consistent with lower-than-expected wave activity.

More elaborate wave distribution profiles (other than Gaussian) may be able to fit the data better. However given our paucity of data points, a more elaborate scheme is unwarranted at present. A future observation with a more densely sampled lightcurve could help to resolve the issue of wave distributions.

Table 2
T58 best-fit parameters.

Wave angle σ (°)	I/F_{max}	X offset (°)	Y offset (°)	χ^2
0.00	3.194	+0.2171	+0.0069	816
0.05	3.786	+0.1695	+0.0153	796
0.10	6.035	+0.0761	+0.0540	767
0.125	19.18	+0.0235	+0.1488	865
0.15	20.85	+0.0770	+0.1719	104
0.18	13.72	+0.1031	+0.1557	1641
0.20	13.88	+0.1192	+0.1752	5823
0.22	12.46	+0.1403	+0.1797	14,070
0.25	10.08	+0.1697	+0.1870	20,650
0.30	8.089	+0.2897	+0.2028	54,510
0.40	6.775	+0.6842	+0.2571	95,309

Such low wave activity is somewhat surprising, given the size of Jingpo Lacus and expected wind thresholds for wave instigation (Lorenz et al., 2010). Nevertheless, the VIMS measurement is consistent with previous observations with RADAR (Stofan et al., 2007; Wye et al., 2009) and VIMS (Brown et al., 2008) that showed smooth liquid surfaces on other Titan lakes.

Lorenz et al. (2010) analyze the lack of wave activity on Titan, pointing to viscous dissipation which may be inhibiting wave activity. Lorenz et al. (2010) also point out that shallow bathymetry can smooth over sea surfaces. While Jingpo Lacus is approximately the same size as south polar Ontario Lacus (Barnes et al., 2009; Turtle et al., 2009), its morphology differs. Jingpo has a

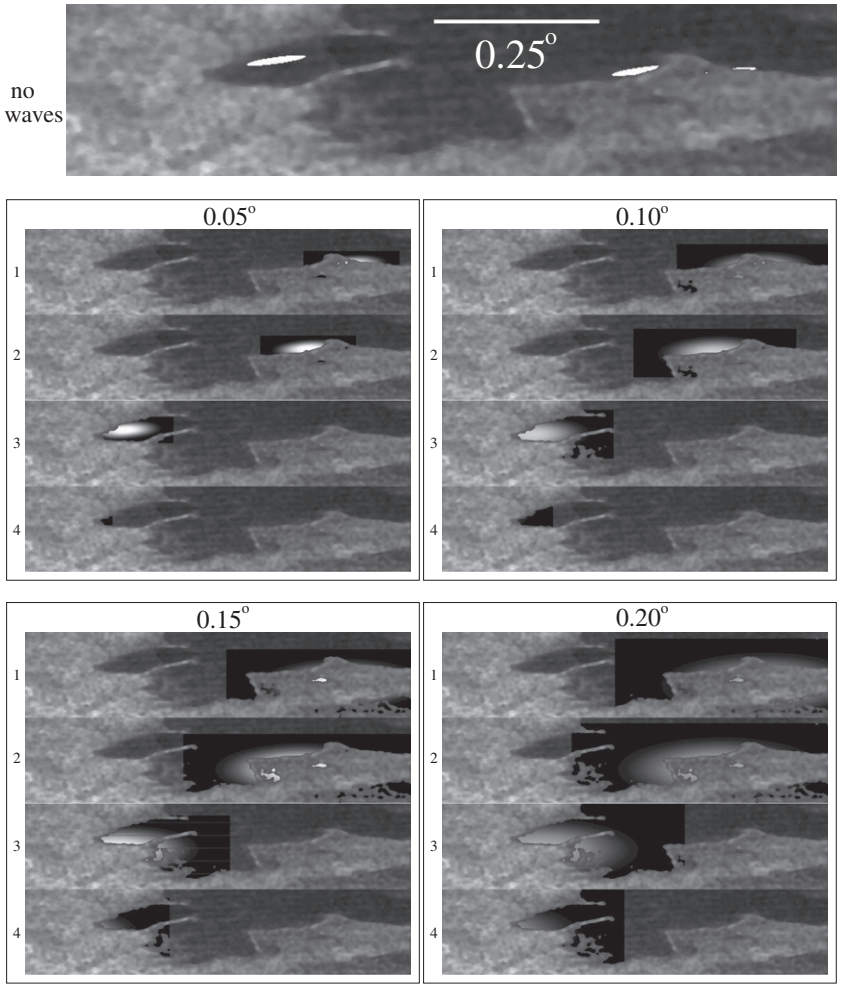

Fig. 11. This figures shows a representation of the specular intensity distribution of the four VIMS T58 observations. In the background is the RADAR SAR view of southwestern Jingpo Lacus from T19, median-filtered (see text). The best-fit intensity distributions are shown for five different wave cases: no waves, or 0° of waves at top; 0.05° Gaussian wave distribution in the upper left; 0.10° Gaussian wave distribution in the upper right; 0.15° Gaussian wave distribution in the lower left; and 0.20° Gaussian wave distribution in the lower right. In the latter four wave cases four different views are shown for each of the four VIMS cubes, labelled 1–4. For the no waves case all four views have been combined into one image since the intensity distributions do not overlap.

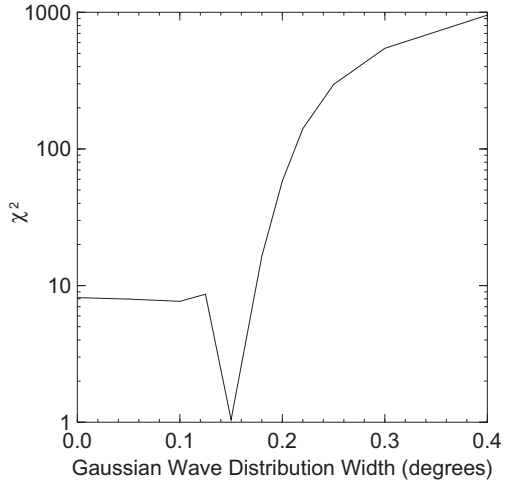

Fig. 12. Chi-squared for the best-fit solution for the 4-point T58 VIMS specular lightcurve as a function of the Gaussian width of the 2-dimensional wave distribution, σ. The minimum at $\sigma = 0.15°$ is suspect (see text); hence we place an upper limit of $\sigma \leqslant 0.15°$ for the waves on Jingpo Lacus at the time of this observation.

complex shoreline of bays and jutting land, while Ontario's shoreline is smooth (Wall et al., 2010), similar to shallow terrestrial playas (Lorenz et al., 2010). Therefore we suspect that the liquid at Jingpo is substantially deeper than at Ontario. Near-shoreline shallows may still affect our measurement (Lorenz et al., 2010, Fig. 2), given that all of our specular footprints are within 3 km of land.

While formally the $\sigma = 0.15°$ wave distribution fits the data the best, we find this fit to be suspect. In order to achieve agreement, the fitting algorithm determined the maximum flux, i.e. the full flux of a specular reflection off of pure liquid, in the $\sigma = 0.15°$ to be greater than $I/F = 18$.

But that value is inconsistent with theory. Soderblom et al. (2010) show that the maximum intensity of a specular reflection from a planetary surface liquid depends on the three parameters: (1) the relative curvature of the reflecting surface; (2) the liquid's index of refraction; and (3) and the atmospheric transmission. Using the flyby geometry for T58, assuming a hydrocarbon liquid for the refractive index, and a the radiative transfer atmosphere from Griffith et al. (2009) and predict a maximum I/F between 1.0 and 3.0 for the VIMS T58 observation. That theoretical value matches our fit for the no-wave case very well. I/F near 18, as from the $\sigma = 0.15°$ fit, is impossible based on present understanding.

Hence while we cannot empirically rule out $\sigma = 0.15°$, we can dismiss this result on theoretical grounds. If we take into account the theoretical specular I/F range of 1–3 from Soderblom et al. (2010), then waves with $\sigma > 0.05$ are ruled out.

So now we have cast doubt on $\sigma = 0.15°$, the only wave distribution that fits point 4. Why does this point not fit the lower-angle wave facet distributions? It could be that our assumption of a 2D Gaussian distribution is at fault. If the true distribution had a wide tail at high wave angles, then that could explain the nonzero specular flux seen for point 4, whose no-waves specular solar image falls entirely on land.

Alternatively, point 4 may be showing specular reflection from unresolved puddles within the specular footprint. If that were the case, then the fill fraction of liquid would need to be ~5% in order to explain the I/F that VIMS observes.

Finally, the land itself may be wetted, similar to but more so than *Huygens* sniffed at its landing site (Niemann et al., 2005). Wetted solids will also show specular reflections, but ones whose intensity is diminished from that of a pure liquid, especially if the solid surface is rough.

The present dataset is sufficiently limited that this single land measurement may be affected by systematic error introduced from the background subtraction. Future observations specifically tailored to generating a specular lightcurve will generate data of high enough quality to allow us to fit for the puddle fraction directly in our models, which would then be less influenced by potential systematic errors.

4. Kraken Mare

During the Titan flyby subsequent to the Jingpo Lacus observation, T59 (2009 July 24), VIMS recorded another specular sequence. This sequence is much less spectacular than that on T58 (Fig. 13). The maximum I/F of the specular signal is lower by a factor of 5.0 due to the spacecraft being farther from Titan. The curvature of Titan's surface causes this effect. The curvature causes an impinging specular reflection to be spread out more than it would be from a flat surface. The effect depends on the surface curvature relative to the angular size of the Sun projected on the curved surface – hence the specular reflection from greater distance has more curvature within a projected solar diameter, and appear dimmer (see a more detailed description of why in Soderblom et al. (2010)). In essence, this is the same reason that objects in your side-view mirrors are larger than they appear.

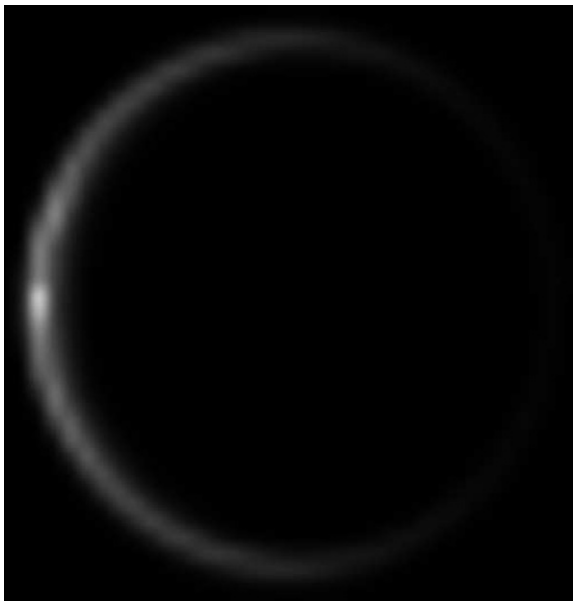

Fig. 13. VIMS 5-μm view of the specular glint off of Kraken Mare on the T59 flyby. *Cassini* was at higher range from Titan than for the T58 specular reflection, and the higher phase angle reduces the intensity as well such that this specular reflection is more than 5 times less intense than that on T58.

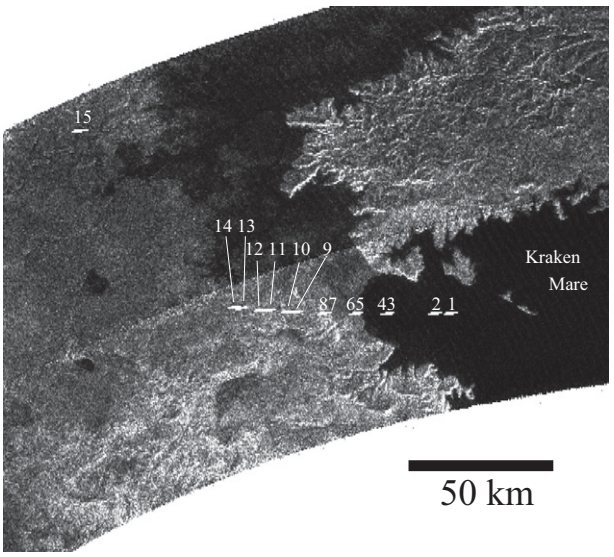

Fig. 14. Locations of the specular solar image from the 15 VIMS T59 observations placed on top of a *Cassini* RADAR T28 SAR view for context. Some images lie on top of one another. The map is a cylindrical projection that has been squeezed in longitude by a factor of 4 in order to more accurately represent shapes and areas.

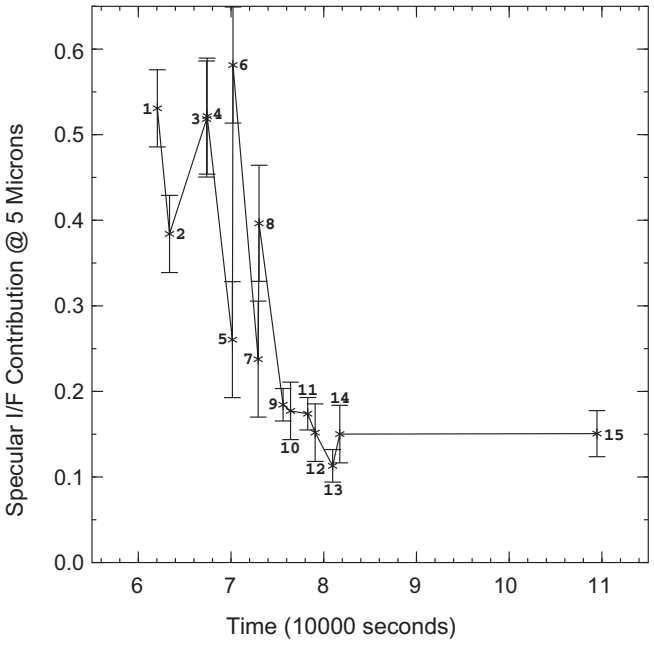

Fig. 15. The VIMS lightcurve from the T59 lightcurve. The total specular flux changes rapidly as a function of time, implying both low wave activity and a mixture of land and liquid surfaces in the specular footprints (see text). We did not calculate errors separately on individual data points; the statistical errors for all of the points are ~0.04 in dimensionless units of I/F.

The specular solar images as viewed from *Cassini* lie in and onshore from northwestern Kraken Mare on T59. The no-wave footprints are shown in Fig. 14.

The T59 sequence has 15 VIMS cubes that contain the specular point. We show a lightcurve derived from these cubes in Fig. 15.

These points span a total of almost 14 h in time. The time separation between data points varies, with the shortest interval being just 64 s between points 3 and 4, points 5 and 6, and then between points 7 and 8. The larger number of points and variable time separations allow us to probe different properties than we did for T58.

The lightcurve is, as one of us (LAS) put it, bizarre. In the 64 s between points 5 and 6, the specular flux rises by more than a factor of 2. A close look at these two data points' solar specular footprints shows that they overlap by 93%. Under the assumptions that we made in Section 3, among these that the specular intensity depends on the fractional land and liquid coverage in the specular footprint, such a large and rapid change in specular intensity is impossible.

Looking back at those assumptions gives us a few possibilities as to what could explain the bizarre T59 specular lightcurve.

Wind gusts: It is possible that active winds were blowing at the time of point 5. These would have incited small capillary waves across the sea surface. If those winds ceased in the intervening 64 s before point 5, those capillary waves may have dissipated sufficiently so as to result in an increased specular reflection. The difficulties with this scenario lie in having near-surface winds change over a few kilometers' distance within 64 s and in dissipating the wave energy rapidly. Regional transient near-surface winds that generate capillary waves are common on Earth, however, and are referred to as "catspaw". High viscosity liquid, as suggested by Lorenz et al. (2010), could dissipate the wave energy. But in that case how would the winds be strong enough to incite the waves in the first place?

Long-wavelength waves: If there are waves on Kraken Mare with wavelength comparable to or larger than the scale of the specular reflection (of order a kilometer), then these waves could be causing the local specular point to dance around on relatively short timescales, resulting in rapidly changing specular intensities. Such a gravity wave travels at a speed

$$c = \sqrt{\frac{g\lambda}{2\pi}\tanh\frac{2\pi d}{\lambda}} \quad (1)$$

where c is the phase speed of the wave, λ is its wavelength, g is the local gravitational acceleration, and d is the liquid depth. If Kraken Mare is more than a few hundred meters deep, then a wave with $\lambda = 1$ km would travel at $c \sim 16$ m/s. It would propagate a 1.02 km over 64 s. Perhaps Kraken Mare, with its larger fetch and probable deeper bathymetry, is different than Ontario. There is also the problem of generating kilometer-scale waves. If they build up from capillary waves, as happens on Earth (Lorenz et al., 2010), then why do not we see the capillary waves? Maybe these long-wavelength waves are incited seismically or tidally instead.

Clouds: Methane cloud activity is common over Titan's north polar lake district (Rodriguez et al., 2009; Brown et al., 2009). If clouds were blocking the specular signal for point 5, and were not blocking point 6 64 s later, then they could account for the difference in specular flux between the two observations. Given the small change in geometry between the two points, and therefore the small shift in the specular solar footprint, this mechanism would require clouds to either dissipate rapidly or to move fast enough to get out of the way in 64 s. Assuming the clouds would have to move 1 km, they would need to be moving at 16 m/s. While winds near Titan's surface were less than 0.2 m/s at the Huygens Landing Site (Lorenz, 2006), they reach 16 m/s near the tropopause at 40 km altitude (Bird et al., 2005). Titan's convective clouds do reach 40 km height (Griffith et al., 2005), so this is a viable mechanism to explain short-timescale specular brightness changes.

None of these hypotheses can be shown to be correct with the present dataset. However a future specular lightcurve with dense temporal sampling of points, at least every 10 s, would either allow us to decide between these mechanisms or could possibly indicate other possibilities. We recommend using at least a 4×4 pixel VIMS aperture, and preferably more like 8×8 in order to facilitate subtracting off the non-specular background signal. VIMS exposure times should be set based on an expected maximum I/F calculated theoretically (Soderblom et al., 2010). Such an observation should be attempted any time that the specular point on Titan lies within 10 km of a liquid body, as sufficiently large waves would allow a specular reflection even if the specular point lies on-shore.

5. Conclusion

Pursuant to the first detection of solar specular reflection from the surface of Titan (Stephan et al., 2010), we develop a model for the intensity of the specular reflection as a function of time. The model accounts for the spacecraft/Titan/Sun geometry to numerically generate the geographic extent of the reflected solar image. We account for waves assuming a 2D Gaussian facet distribution. We represent the net reflection as a convolution of the solar image and the point-source wave smearing effect. Using *Cassini* RADAR for reference, we take locations with SAR single-scattering cross-section σ_0 less than 0.05 to be sea, and those with radar reflectance above 0.05 to be land.

This model can reproduce the VIMS 5-μm photometric lightcurve for the T58 specular reflection adequately for wave slopes $\sigma \leqslant 0.15°$. Allowing the theoretical specular reflection properties from Soderblom et al. (2010) to constrain the model brings that upper limit down to $\sigma \leqslant 0.05°$. All factors considered, the zero-wave-slope scenario seems to be the most likely. The specular point for T58 lies in the southwestern portion of Jingpo Lacus, a roughly Ontario Lacus-sized northern lake. The final photometric point from this sequence has a specular point that lies on land. That point does not match the model. Possible reasons include a too-simplified wave facet distribution, wetted land surface, or unresolved puddles.

VIMS saw another, less intense specular reflection during the T59 flyby. That specular point was in northwestern Kraken Mare. The resulting lightcurve cannot be understood in terms of the model that we developed for T58. The specular reflection intensity changes by over a factor of 2.0 in just 64 s. We suggest three hypotheses for such rapid variation in the specular intensity: changing wind conditions, kilometer-plus wavelength waves, and moving clouds.

The utility of these specular observations leads us to recommend that more observations be made whenever the opportunity presents itself on future flybys. Such observations should be made with an aperture large enough to allow confident background subtraction and should acquire photometric points every 10 s. This type of observation could verify the unusual variability over Titan's larger Maria, allowing us to determine whether it is caused by wave activity. These observations could then be used to back out the near-surface wind environment, as has been done on the Earth (e.g. Fox et al., 2007).

Acknowledgment

The authors acknowledge support from the NASA/ESA *Cassini* project.

References

Acton, C.H., 1999. SPICE products available to the planetary science community. In: Lunar and Planetary Institute Conference Abstracts, pp. 1233–1234.

Agol, E., Cowan, N.B., Knutson, H.A., Deming, D., Steffen, J.H., Henry, G.W., Charbonneau, D., 2010. The climate of HD 189733b from fourteen transits and eclipses measured by Spitzer. ArXiv e-prints.

Barnes, J.W., Fortney, J.J., 2004. Transit detectability of ring systems around extrasolar giant planets. Astrophys. J. 616, 1193–1203.
Barnes, J.W. et al., 2009. Shoreline features of Titan's Ontario Lacus from Cassini/VIMS observations. Icarus 201, 217–225.
Barnes, J.W. et al., 2009. VIMS spectral mapping observations of Titan during the Cassini prime mission. Planet. Space Sci. 57, 1950–1962.
Bird, M.K. et al., 2005. The vertical profile of winds on Titan. Nature 438, 800–802.
Brown, R.H., Soderblom, L.A., Soderblom, J.M., Clark, R.N., Jaumann, R., Barnes, J.W., Sotin, C., Buratti, B., Baines, K.H., Nicholson, P.D., 2008. The identification of liquid ethane in Titan's Ontario Lacus. Nature 454, 607–610.
Brown, M.E., Schaller, E.L., Roe, H.G., Chen, C., Roberts, J., Brown, R.H., Baines, K.H., Clark, R.N., 2009. Discovery of lake-effect clouds on Titan. Geophys. Res. Lett. 36, 1103.
Campbell, D.B., Black, G.J., Carter, L.M., Ostro, S.J., 2003. Radar evidence for liquid surfaces on Titan. Science 302, 431–434.
Cowan, N.B., the EPOXI Team, et al., 2009. Alien maps of an ocean-bearing world. Astrophys. J. 700, 915–923.
Cox, C., Munk, W., 1954. Measurement of the roughness of the sea surface from photographs of the Sun's glitter. J. Opt. Soc. Am. 44, 838–850.
Fox, D., Gonzalez, E., Kahn, R., Martonchik, J., 2007. Near-surface wind speed retrieval from space-based, multi-angle imaging of ocean Sun glint patterns. Remote Sens. Environ. 107 (1–2), 223–231. Multi-angle Imaging SpectroRadiometer (MISR) Special Issue.
Fussner, S., 2006. Search for 938 nm Specular Enhancement on Titan. Masters Thesis, University of Arizona, Tucson, AZ.
Griffith, C.A. et al., 2005. The evolution of Titan's mid-latitude clouds. Science 310, 474–477.
Griffith, C.A., Penteado, P., Rodriguez, S., LeMouélic, S., Baines, K.H., Buratti, B., Clark, R., Nicholson, P., Jaumann, R., Sotin, C., 2009. Characterization of clouds in Titan's tropical atmosphere. Astrophys. J. 702, L105–L109.
Knutson, H.A., Charbonneau, D., Noyes, R.W., Brown, T.M., Gilliland, R.L., 2007. Using stellar limb-darkening to refine the properties of HD 209458b. Astrophys. J. 655, 564–575.
Lorenz, R.D., 2006. Thermal interactions of the Huygens probe with the Titan environment: Constraint on near-surface wind. Icarus 182, 559–566.
Lorenz, R.D., Jackson, B., Hayes, A., 2010. Racetrack and Bonnie Claire: Southwestern US playa lakes as analogs for Ontario Lacus, Titan. Planet. Space Sci. 58, 724–731.
Lorenz, R.D., Newman, C., Lunine, J.I., 2010. Threshold of wave generation on Titan's lakes and seas: Effect of viscosity and implications for Cassini observations. Icarus 207 (2), 932–937.
Niemann, H.B. et al., 2005. The abundances of constituents of Titan's atmosphere from the GCMS instrument on the Huygens probe. Nature 438, 779–784.
Oakley, P.H.H., Cash, W., 2009. Construction of an Earth model: Analysis of exoplanet light curves and mapping the next Earth with the new worlds observer. Astrophys. J. 700, 1428–1439.
Press, W.H., Teukolsky, S.A., Vetterling, W.T., Flannery, B.P., 2007. Numerical Recipes: The Art of Scientific Computing. University Press, Cambridge.
Rodriguez, S. et al., 2009. Global circulation as the main source of cloud activity on Titan. Nature 459, 678–682.
Seager, S., Mallén-Ornelas, G., 2003. A unique solution of planet and star parameters from an extrasolar planet transit light curve. Astrophys. J. 585, 1038–1055.
Soderblom, J.M. et al., 2010. Modeling specular reflections from hydrocarbon lakes on the surface of Titan. Icarus, submitted for publication.
Stephan, K. et al., 2010. Specular reflection on Titan: Liquids in Kraken Mare. Geophys. Res. Lett. 37, 7104.
Stiles, B.W., The Cassini RADAR Team, et al., 2008. Determining Titan's spin state from Cassini RADAR images. Astron. J. 135, 1669–1680.
Stofan, E.R. et al., 2007. The lakes of Titan. Nature 445, 61–64.
Turtle, E.P., Perry, J.E., McEwen, A.S., Del Genio, A.D., Barbara, J., West, R.A., Dawson, D.D., Porco, C.C., 2009. Cassini imaging of Titan's high-latitude lakes, clouds, and south-polar surface changes. Geophys. Res. Lett. 36, 2204.
Wall, S. et al., 2010. Active shoreline of Ontario Lacus, Titan: A morphological study of the lake and its surroundings. Geophys. Res. Lett. 37, 5202.
West, R.A., Brown, M.E., Salinas, S.V., Bouchez, A.H., Roe, H.G., 2005. No oceans on Titan from the absence of a near-infrared specular reflection. Nature 436, 670–672.
Williams, D.M., Gaidos, E., 2008. Detecting the glint of starlight on the oceans of distant planets. Icarus 195, 927–937.
Wye, L.C., Zebker, H.A., Lorenz, R.D., 2009. Smoothness of Titan's Ontario Lacus: Constraints from Cassini RADAR specular reflection data. Geophys. Res. Lett. 36, 16201.
Zebker, H.A., Stiles, B., Hensley, S., Lorenz, R., Kirk, R.L., Lunine, J., 2009. Size and shape of Saturn's moon Titan. Science 324, 921–923.